

Formation of ZnO_4 Tetrahedra and ZnO_6 Octahedra in TeZnO_3 Synthesized under High Pressure

Jianhong Dai,^{†,‡} Xudong Shen,^{†,‡} Zhehong Liu,^{†,‡} Qing Zhao,^{†,‡} Xiao Wang,^{†,‡} Cheng Dong,^{†,‡} Yuecheng Bian,[§] Wei Ding,[§] Zhigao Sheng,[§] Masaki Azuma,^{||} and Youwen Long^{*,†,‡,||}

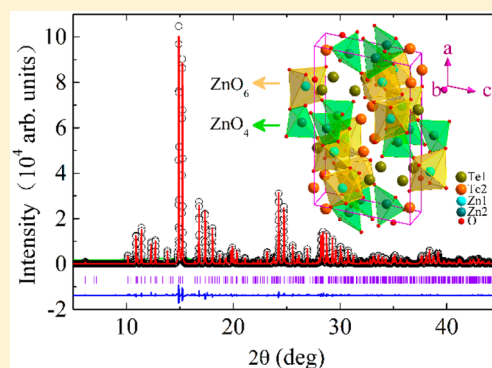
[†]Beijing National Laboratory for Condensed Matter Physics, Institute of Physics, Chinese Academy of Sciences, Beijing 100190, China

[‡]School of Physics, University of Chinese Academy of Sciences, Beijing 100049, China

[§]Anhui Key Laboratory of Condensed Matter Physics at Extreme Conditions, High Magnetic Field Laboratory, Chinese Academy of Sciences, Hefei 230031, P. R. China

^{||}Laboratory for Materials and Structures, Tokyo Institute of Technology, 4259 Nagatsuta, Midori, Yokohama 226-8503, Japan

ABSTRACT: A new TeZnO_3 phase was synthesized by high-pressure techniques. Different from the ambient-pressure orthorhombic phase composed of ZnO_5 units, the current high-pressure one crystallizes to a monoclinic structure with space group $P2_1/n$. Moreover, both ZnO_4 tetrahedral and ZnO_6 octahedral polyhedra are found to occur in this new phase, providing a unique Zn-based material system that simultaneously possesses two distinct coordinated units. Because the outermost orbitals are fully occupied for both Zn^{2+} and Te^{4+} , the compound exhibits diamagnetism and strong insulating behavior with a wide bandgap as large as 6.0 eV. Dielectric constant and specific heat measurements show a broad anomaly around 240 K. Low-temperature synchrotron X-ray diffraction reveals an isostructural phase transition at this temperature.



I. INTRODUCTION

ABO_3 perovskites exhibit very flexible structural behaviors and a wide variety of interesting physical properties because of the versatile A–B ionic and charge combinations, where the A site is usually occupied by alkaline, alkaline earth, or rare earth metals with a larger ionic radius to sustain the crystal construction, whereas transition metals often accommodate the B site that dominates the electronic properties of the compounds.^{1–5} Compared with the $\text{A}^{2+}\text{B}^{4+}\text{O}_3$ -type and $\text{A}^{3+}\text{B}^{3+}\text{O}_3$ -type charge formats, the amount of perovskite with $\text{A}^{4+}\text{B}^{2+}\text{O}_3$ -type charge combination is very rare.^{6–8} To date, only a few compounds such as PbNiO_3 and the chalcogen family of $\text{Ch}^{4+}\text{M}^{2+}\text{O}_3$ (Ch = Se or Te; M = Mg, Mn, Co, Ni, or Cu) are found to crystallize in this kind of charge format.^{9–16} Because of the smaller size of Se^{4+} and Te^{4+} ions, the M–O–M bonding in $\text{Ch}^{4+}\text{M}^{2+}\text{O}_3$ perovskites is heavily bent so that the bond angles are as small as 120–130°. This value is located at the phase boundary of the Goodenough–Kanamori (GK) rules that are frequently used to evaluate ferromagnetic or antiferromagnetic superexchange interactions in 3d transition-metal oxides based on the B–O–B bond angles.^{17,18} Therefore, members of the ChMO_3 family such as SeCuO_3 and TeCuO_3 are regarded as prototype material systems for examining the validity of the GK rules. For example, with the Te concentration (x) increasing from 0 to 1, the solid solution of $\text{Se}_{1-x}\text{Te}_x\text{CuO}_3$ gradually changes from ferromagnetism to antiferromagnetism accompanied by an average Cu–O–Cu

bond angle variation from 121.8° to 130.0°.^{19,20} Moreover, considerable magnetodielectric effects arising from spin fluctuations are also found to occur in Se/TeCuO_3 .²¹

Because of the strong octahedral distortions in $\text{Ch}^{4+}\text{M}^{2+}\text{O}_3$, high pressure (2–8 GPa) is necessary to stabilize the perovskite structure during the synthesis. As far as the end member of the 3d transition-metal Zn is concerned, the SeZnO_3 perovskite was successfully prepared under 4.5 GPa and 1023 K. However, there is no report for the high-pressure synthesis for TeZnO_3 . Instead, a TeZnO_3 single crystal is grown at ambient pressure.^{22,23} As shown in Figure 2a, different from the BO_6 octahedral coordination in perovskite, the ambient-pressure synthesized TeZnO_3 (AP-TZO) possesses unusual ZnO_5 polyhedral units with the Zn–O bond lengths changing from 1.96 to 2.27 Å (see Table 1). In general, ZnX_4 (X stands for a coordinated atom) tetrahedra are often found to occur in most Zn-based compounds such as sphalerite ZnS , wurtzite ZnO , spinel $(\text{Al/Fe})_2\text{ZnO}_4$, etc.^{24–26} In addition, in $\text{A}_2\text{BB}'\text{O}_6$ -type double perovskites, the Zn^{2+} can also be introduced into the B site to form ZnO_6 octahedra as observed in $\text{La}_2\text{ZnIrO}_6$, $\text{Ba}_2\text{ZnIrO}_6$, and $\text{Sr}_2\text{ZnIrO}_6$.^{27–30} Until now, in the zinc compounds, ZnX_4 tetrahedra and ZnX_6 octahedra have not been found to coexist.

Received: April 9, 2018

Published: May 16, 2018

Table 1. Refined Structural Parameters of the Newly Synthesized HP-TZO and Those of the AP-TZO Reported in ref 23

	AP-TZO			HP-TZO		
space group	<i>Pbca</i>			<i>P2₁/n</i>		
lattice constants (Å)	<i>a</i> = 7.36	<i>b</i> = 6.38	<i>c</i> = 12.32	<i>a</i> = 12.9707(1)	<i>b</i> = 5.2966(1)	<i>c</i> = 7.9087(1)
angles (deg)	α = 90	β = 90	γ = 90	α = 90	β = 99.813(0)	γ = 90
	AP-TZO			HP-TZO		
	<i>x</i>	<i>y</i>	<i>z</i>	<i>x</i>	<i>y</i>	<i>z</i>
Te(1)	0.062(7)	0.092(6)	0.143(5)	0.2921(1)	0.2679(3)	0.9504(1)
Te(2)	–	–	–	0.5797(1)	0.7820(3)	0.4620(2)
Zn(1)	0.109(7)	0.121(8)	0.409(5)	0.3359(1)	0.7458(7)	0.1779(2)
Zn(2)	–	–	–	0.5242(1)	0.2809(6)	0.1622(2)
O(1)	0.472(8)	0.199(3)	0.224(6)	0.3951(9)	0.0852(2)	0.1006(15)
O(2)	0.039(0)	0.342(9)	0.067(1)	0.6161(10)	0.4416(18)	0.0162(16)
O(3)	0.156(3)	0.473(9)	0.409(7)	0.2313(8)	0.4128(18)	0.1352(14)
O(4)	–	–	–	0.4844(8)	0.5699(18)	0.3166(13)
O(5)	–	–	–	0.2023(9)	0.9079(18)	0.9827(15)
O(6)	–	–	–	0.3944(8)	0.0017(18)	0.7087(14)
Te(1)–O (Å)	1.86, 1.88, 1.89, 2.71			1.895, 1.933, 1.936, 2.271, 2.816		
Te(2)–O (Å)	–			1.845, 1.866, 1.904, 2.727, 2.780		
Zn(1)–O (Å)	1.96, 2.00, 2.02, 2.11, 2.27			2.041, 2.087, 2.014, 2.215, 2.251, 2.282		
Zn(2)–O (Å)	–			1.958, 1.987, 2.007, 2.077, 2.566		

In this paper, a new TeZnO_3 phase prepared under high pressure (HP-TZO) is obtained. In sharp contrast to the AP-TZO phase, the high-pressure one is built from ZnO_4 and ZnO_6 units, providing the first example of a zinc compound that simultaneously includes ZnO_4 tetrahedral and ZnO_6 octahedral coordination polyhedra. This oxide shows diamagnetic behavior with a wide insulating energy gap of ~ 6.0 eV. The dielectric constant and specific heat experience a broadening anomaly around 240 K, suggesting an isostructural variation as illustrated by low-temperature X-ray diffraction.

II. EXPERIMENTAL DETAILS

Polycrystalline HP-TZO was prepared using stoichiometric ZnO (Alfa, 99.9%) and TeO_2 (Alfa, 99.9%) as starting materials. The reactants were finely mixed in an agate mortar and then sealed into a gold capsule that was 4.2 mm in diameter and 5.0 mm in height. The capsule was treated at 5 GPa and 1023 K for 40 min on a cubic-anvil-type high-pressure apparatus. At the completion of heating, the reaction was quenched to ambient conditions, and then a pale green bulk was obtained.

High-resolution synchrotron X-ray diffraction (SXR) was performed at beamline BL02B2 of SPring-8 at different temperatures. The wavelengths we used were 0.773 Å at room temperature and 0.421 Å at lower temperatures. The crystal structure of HP-TZO was determined by the direct method using the EXPO2014 program.³¹ The detailed crystal structure was then refined by the Rietveld method through the GSAS program.³² Magnetic susceptibility and magnetization were measured using a superconducting quantum interference device magnetometer (Quantum Design, VSM-7T). The temperature dependence of magnetic susceptibility data was collected at 0.1 T and 2–300 K. The field dependence of magnetization was measured at 2, 50, and 300 K between -1 and 1 T. An ultraviolet–visible–near-infrared spectrophotometer (UV–vis–NIR, Cary-5E) was used to explore the optical spectrum of the polycrystalline HP-TZO bulk. The dielectric constant was measured on a pellet that was 3.2 mm in diameter and 0.24 mm in height using an Agilent E4980A Precision LCR Meter at different frequencies. An alternating voltage of 1.0 V was applied to produce inductive charge. Specific heat data were collected on a physical property measurement system (Quantum Design, PPMS-9T).

III. RESULTS AND DISCUSSION

Figure 1 shows the SXR pattern of HP-TZO measured at room temperature. The EXPO2014 program was used for the

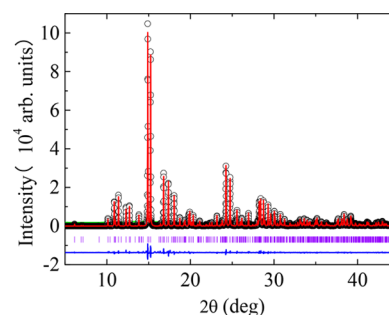


Figure 1. Synchrotron X-ray diffraction pattern of HP-TZO measured at room temperature. Observed (black circles), calculated (red line), and difference (blue line) profiles are shown together with the allowed Bragg reflections (ticks) in the $P2_1/n$ space group.

crystal structure determination. The first 25 peaks were used by N-TREOR for the indexing, and a satisfactory indexing result ($M_{20} = 34$) was obtained with a monoclinic cell ($a = 12.971$ Å, $b = 5.2963$ Å, $c = 7.9091$ Å, and $\beta = 99.82^\circ$). The space group derived from the extinction rules is $P2_1/n$ (No. 14), and the preliminary atomic positions are determined by direct methods. Furthermore, according to these results, the Rietveld refinement gives desirable resolution for the detailed structural parameters with the following satisfactory factors: $R_{wp} = 3.60\%$, $R_p = 2.76\%$, and $\chi^2 = 1.2$. Table 1 lists the refined structural parameters for HP-TZO as well as those reported for AP-TZO in ref 23. By comparison, the usage of high-pressure synthesis conditions changes the crystal symmetry from orthorhombic $Pbca$ at ambient pressure to monoclinic $P2_1/n$, giving rise to a sharp decrease in unit cell volume per formula of $\sim 7.5\%$. The uniform Te and Zn sites in $Pbca$ separate into two distinct ones in $P2_1/n$, which accompanies the reduction in symmetry. Figure 2a shows the schematic crystal structure of AP-TZO. Each Te is coordinated by three nearest neighbor O atoms with the Te–O

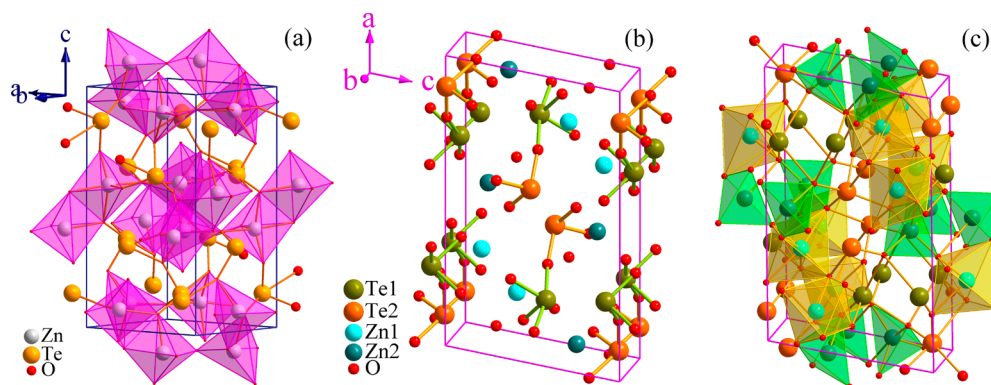


Figure 2. (a) Schematic crystal structure of AP-TZO. ZnO_5 polyhedra are colored magenta. (b) Corner-sharing TeO_3 and TeO_4 polymerization units in HP-TZO at the Te2 and Te1 sites, respectively. (c) Schematic crystal structure of HP-TZO composed of ZnO_6 octahedral (yellow) and ZnO_4 tetrahedral (green) units at the Zn1 and Zn2 sites, respectively.

distance changing from 1.86 to 1.89 Å, while each Zn is coordinated by five O atoms with the Zn–O distance changing from 1.96 to 2.27 Å. Therefore, ZnO_5 polyhedra are formed in AP-TZO. On the other hand, in HP-TZO, the three shortest Te2–O distances (1.845–1.904 Å) are also found at the Te2 site, whereas the Te1 site can be regarded as four-coordinated O atoms with three shorter Te1–O bond lengths from 1.895 to 1.936 Å and one longer bond length of 2.271 Å (see Table 1 and Figure 2b).³³ On the basis of the theory of band valence sum, the valence state is calculated to be +3.95 for Te1 and +3.99 for Te2. Both are very close to the nominal +4 state.³⁴ As far as the coordination of Zn is concerned in HP-TZO, it exhibits essential differences compared to that of AP-TZO. As presented in Table 1, there are six shortest Zn1–O bond lengths (2.041–2.282 Å), forming a ZnO_6 octahedron at the Zn1 site. In contrast, the coordinated number of Zn2 is reduced to 4 because the fifth shortest Zn2–O distance (2.566 Å) is much longer than the four shortest ones (1.958–2.077 Å). Therefore, a ZnO_4 tetrahedron is formed at the Zn2 site, as shown in Figure 2c. Moreover, the bond valence sum calculations give an average valence state of Zn of +1.83 (+1.88 for Zn1 and +1.78 for Zn2), agreeing with the expected +2 state. These results indicate that the current HP-TZO forms a new structure that is essentially different from that of AP-TZO as well as the octahedral corner-sharing perovskite. As shown in Figure 2c, in HP-TZO, each ZnO_6 unit connects with two neighboring ZnO_6 and three ZnO_4 units by sharing corners, giving rise to the occurrence of a dangling O atom without linking with any other polyhedra. For each ZnO_4 unit, it is also corner-sharing with three neighboring ZnO_6 octahedra and leaves a dangling O atom.

Figure 3a shows the temperature dependence of magnetic susceptibility of the HP-TZO measured at 0.1 T with zero-field cooling (ZFC) and field cooling (FC) modes. Apparently, the ZFC and FC susceptibility curves overlap completely. Moreover, both show negative susceptibility values in 4–300 K, indicating the presence of diamagnetic behavior, as confirmed by the magnetization measurements shown in the inset of Figure 3a.³⁵ This is consistent with the Te^{4+} ($4d^{10}5s^2$) and Zn^{2+} ($3d^{10}$) valence states mentioned above. As expected from the Landau diamagnetic theory, the magnitude of susceptibility is nearly temperature independent above 50 K in the current HP-TZO. Note that the slightly positive susceptibility values observed below 4 K should be attributed to a tiny undiscernable impurities which may exist in the starting materials. Since the

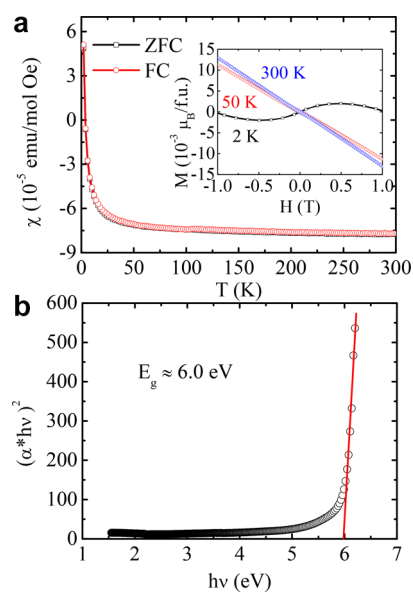


Figure 3. (a) Temperature dependence of the magnetic susceptibility of HP-TZO measured at 0.1 T. The inset shows the magnetization measured at 2, 50, and 300 K. (b) Tauc plot of the optical spectrum for HP-TeZnO₃ measured at room temperature.

outmost orbitals for both Te^{4+} and Zn^{2+} are fully occupied, strong electrical insulating behavior is expected to find in the HP-TZO. Figure 3b shows the Tauc plot of the optical spectrum measured at room temperature. With the fitting result based on the equation $(\alpha h\nu)^2 = A(h\nu - E_g)$,³⁶ it is found that the HP-TZO has a wide energy gap as large as 6.0 eV, which is well consistent with the electronic configurations of Te^{4+} and Zn^{2+} .

The strong insulating feature of HP-TZO allows us to characterize the intrinsic dielectric properties. Figure 4a presents the temperature dependence of the relative dielectric constant measured in 2–300 K at different frequencies. The dielectric constant gradually increases with increasing temperature and experiences a broad anomaly near 240 K at 1 kHz. Moreover, this anomaly shifts toward higher temperatures when the measurement frequency increases. Because the dielectric loss we obtained is <0.6% in the whole temperature region, the dielectric anomaly may suggest an intrinsic variation in HP-TZO. The specific heat (C_p) as a function of temperature is thus measured. Corresponding to the dielectric

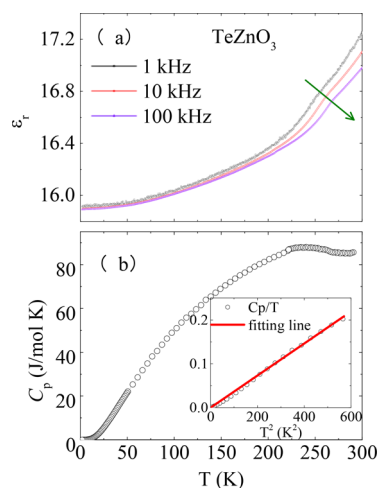


Figure 4. Temperature dependence of (a) relative dielectric constant ϵ_r , measured at different frequencies and (b) specific heat C_p for HP-TZO. The inset shows the fitting result for a specific heat below 24 K using the function $C_p/T = \alpha T^2$.

change, a wide hump is also observed in C_p near 240 K, as shown in Figure 4b. At low temperatures (<24 K), the specific heat data can be well fitted based on the Debye mode. The inset of Figure 4b shows the fitting result using the function $C_p/T = \alpha T^2$, yielding a coefficient α of $0.37 \pm 0.07 \text{ mJ mol}^{-1} \text{ K}^{-4}$. According to the α value, the Debye temperature of HP-TZO is calculated to be 174.5 K, which is comparable with those obtained in many other ABO_3 perovskite oxides.³⁷ Note that, although the stereochemical effects of the $5s^2$ lone-pair electrons in Te^{4+} ions can induce a ferroelectric phase transition,^{38–40} this possibility is ruled out in HP-TZO by the pyroelectric current measurement (not shown here). In the temperature window we measured (2–300 K), there is not any trace of electric polarization.

To clarify the origin for the phase transition occurring around 240 K, low-temperature SXR D was performed on HP-TZO. Figure 5a shows some representative SXR D patterns at different temperatures. Obviously, all the peaks systematically shift toward larger angles on cooling because of volume contraction (for clarity, see the inset of Figure 5a). It means that there is no crystal symmetry change as the temperature decreases to 160 K. However, when the normalized structural parameters are plotted as a function of temperature (Figure 5b), one finds remarkable variations in the lattice parameters and unit cell volume around 240 K, while intersection angle β between the a - and c -axes smoothly crosses the transition temperature. These results reveal that an isostructural phase transition takes place in HP-TZO near 240 K, which is responsible for the variations observed in the dielectric constant and heat capacity. In spite of the unchanged macroscopic crystal symmetry ($P2_1/n$), some underlying polyhedral distortions can trigger the isostructural phase transition.

IV. CONCLUSION

In summary, we succeeded in synthesizing a new phase of TeZnO_3 under high pressure with Zn^{2+} and Te^{4+} charge states. Using high-resolution synchrotron X-ray diffraction technology, the crystal structure of HP-TZO has been determined. Different from the orthorhombic ambient-pressure phase that is built from ZnO_5 units, the high-pressure phase crystallizes to monoclinic symmetry with space group $P2_1/n$, where both

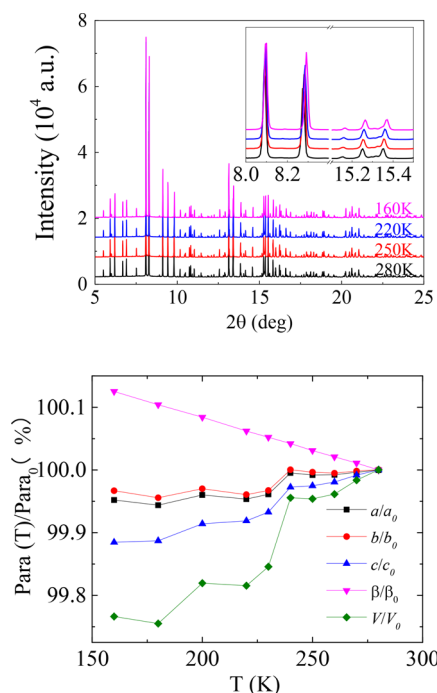


Figure 5. (a) Representative low-temperature synchrotron X-ray diffraction patterns of HP-TZO recorded at different temperatures. The inset shows a magnified view of the systematical shift of the diffraction peaks. (b) Normalized structural parameters (Para.) as a function of temperature. Para₀ stands for the parameters obtained at 280 K.

ZnO_4 tetrahedra and ZnO_6 octahedra are found to occur simultaneously. Because of the fully occupied orbitals for both Te^{4+} ($4d^{10}5s^2$) and Zn^{2+} ($3d^{10}$), HP-TZO shows Landau diamagnetic behavior with nearly constant negative susceptibility above 50 K. The ultraviolet spectroscopy study gives a wide energy gap as large as 6.0 eV, revealing the strong insulating feature. Although $5s^2$ lone-pair electrons exist in Te^{4+} ions, no electric polarization is observed in the range of 2–300 K. The dielectric and specific heat measurements both show an anomaly near 240 K. Furthermore, low-temperature SXR D reveals an isostructural phase transition taking place around this critical temperature, where the macroscopic crystal symmetry is unchanged but the normalized lattice parameters and unit cell volume experience remarkable variations.

■ AUTHOR INFORMATION

Corresponding Author

*E-mail: ywlong@iphy.ac.cn.

ORCID

Masaki Azuma: 0000-0002-8378-321X

Youwen Long: 0000-0002-8587-7818

Notes

The authors declare no competing financial interest.

■ ACKNOWLEDGMENTS

This work was supported by the National Natural Science Foundation of China (Grants 11574378 and 51772324), the 973 Project of the Ministry of Science and Technology of China (Grants 2014CB921500 and 2018YFA0305700), and the Chinese Academy of Sciences (Grants YZ201555, QYZDB-SSW-SLH013, XDB07030300, and GJHZ1773). Y.L. was

partially supported by the World Research Hub Initiative, Institute of Innovative Research, Tokyo Institute of Technology, and Collaborative Research Projects, Laboratory for Materials and Structures, Tokyo Institute of Technology. JSPS and CAS under the Japan-China Scientific Cooperation Program. The synchrotron radiation experiments were performed at SPring-8 with the approval of the Japan Synchrotron Radiation Research Institute (2017A1388).

REFERENCES

- (1) Goldschmidt, V. M. The laws of crystal chemistry. *Naturwissenschaften* **1926**, *14*, 477.
- (2) Giaquinta, D. M.; zur Loye, H.-C. Structural Predictions in the ABO₃ Phase Diagram. *Chem. Mater.* **1994**, *6*, 365–372.
- (3) Rodgers, J. A.; Williams, A. J.; Attfield, J. P. High-pressure/High-temperature Synthesis of Transition Metal Oxide Perovskites. *Z. Naturforsch., B: J. Chem. Sci.* **2006**, *61*, 1515–1526.
- (4) Belik, A. A.; Matsushita, Y.; Tanaka, M.; Takayama-Muromachi, E. Crystal Structures and Properties of Perovskites ScCrO₃ and InCrO₃ with Small Ions at the A Site. *Chem. Mater.* **2012**, *24*, 2197–2203.
- (5) Belik, A. A.; Yi, W. High-Pressure Synthesis, Crystal Chemistry and Physics of Perovskites with Small Cations at the A Site. *J. Phys.: Condens. Matter* **2014**, *26*, 163201.
- (6) Ishiwata, S.; Azuma, M.; Takano, M. Structure and Physical Properties of Perovskite Bi_{0.8}Pb_{0.2}NiO₃ in Unusual Valence State A⁴⁺B²⁺O₃. *Chem. Mater.* **2007**, *19*, 1964–1967.
- (7) Yoshimura, M.; Nakamura, T.; Sata, T. Preparation and Lattice Distortion of Perovskite-Type Compounds A²⁺R⁴⁺O₃ (A = Ba, Sr R = Ce, Pr, Tb). *Chem. Lett.* **1973**, *2*, 923–928.
- (8) Ishiwata, S.; Azuma, M.; Takano, M.; Nishibori, E.; Takata, M.; Sakata, M.; Kato, K. High pressure synthesis, crystal structure and physical properties of a new Ni(II) perovskite BiNiO₃. *J. Mater. Chem.* **2002**, *12*, 3733–3737.
- (9) Inaguma, Y.; Tanaka, K.; Tsuchiya, T.; Mori, D.; Katsumata, T.; Ohba, T.; Hiraki, K.; Takahashi, T.; Saitoh, K. Synthesis, Structural Transformation, Thermal Stability, Valence State, and Magnetic and Electronic Properties of PbNiO₃ with Perovskite and LiNbO₃-Type Structures. *J. Am. Chem. Soc.* **2011**, *133*, 16920–16929.
- (10) Kohn, K.; Inoue, K.; Horie, O.; Akimoto, S. I. Crystal Chemistry of MSeO₃ and MTeO₃ (M = Mg, Mn, Co, Ni, Cu, and Zn). *J. Solid State Chem.* **1976**, *18*, 27–31.
- (11) Kohn, K.; Akimoto, S. I.; Inoue, K.; Asai, K.; Horie, O. Crystal Structure and Magnetic Properties of MnSeO₃, CoSeO₃, NiSeO₃ and CuSeO₃. *J. Phys. Soc. Jpn.* **1975**, *38*, 587.
- (12) Kohn, K.; Akimoto, S. I.; Uesu, Y.; Asai, K. Crystal Structure and Magnetic Properties of MnTeO₃, CoTeO₃ and NiTeO₃. *J. Phys. Soc. Jpn.* **1974**, *37*, 1169.
- (13) Villesuzanne, A.; Whangbo, M.-H.; Subramanian, M. A.; Matar, S. F. Spin Dimer and Electronic Band Structure Analyses of the Ferromagnetism versus Antiferromagnetism in SeCuO₃ and TeCuO₃. *Chem. Mater.* **2005**, *17*, 4350–4355.
- (14) Muñoz, A.; Alonso, J. A.; Martínez-Lope, M. J.; Morán, E.; Escamilla, R. Synthesis and study of the crystallographic and magnetic structure of SeCoO₃. *Phys. Rev. B: Condens. Matter Mater. Phys.* **2006**, *73*, 104442.
- (15) Muñoz, A.; Alonso, J. A.; Martínez-Lope, M. J.; Falcon, H.; García-Hernández, M.; Morán, E. High-pressure synthesis and study of the crystal and magnetic structure of the distorted SeNiO₃ and SeMnO₃ perovskites. *Dalton Trans.* **2006**, *41*, 4936–4943.
- (16) Martínez-Lope, M. J.; Retuerto, M.; Alonso, J. A.; Sánchez-Benítez, J.; Fernández-Díaz, M. T. High-pressure synthesis and neutron diffraction investigation of the crystallographic and magnetic structure of TeNiO₃ perovskite. *Dalton Trans.* **2011**, *40*, 4599–4604.
- (17) Goodenough, J. B.; Loeb, A. L. Theory of Ionic Ordering, Crystal Distortion, and Magnetic Exchange Due to Covalent Forces in Spinels. *Phys. Rev.* **1955**, *98*, 391–407.
- (18) Kanamori, J. Superexchange Interaction and Symmetry Properties of Electron Orbitals. *J. Phys. Chem. Solids* **1959**, *10*, 87–98.
- (19) Íñiguez, J.; Yildirim, T. Unusual structural tuning of magnetism in cuprate perovskites. *Phys. Rev. B: Condens. Matter Mater. Phys.* **2005**, *71*, 180415-R.
- (20) Subramanian, M. A.; Ramirez, A. P.; Marshall, W. J. Structural Tuning of Ferromagnetism in a 3D Cuprate Perovskite. *Phys. Rev. Lett.* **1999**, *82*, 1558.
- (21) Lawes, G.; Ramirez, A. P.; Varma, C. M.; Subramanian, M. A. Magnetodielectric Effects from Spin Fluctuations in Isostructural Ferromagnetic and Antiferromagnetic Systems. *Phys. Rev. Lett.* **2003**, *91*, 257208.
- (22) Hanke, K. Zinktellurit: Kristallstruktur und Beziehungen zu einigen Seleniten. *Naturwissenschaften* **1967**, *54*, 199.
- (23) Nawash, J. M.; Lynn, K. G. ZnTeO₃ crystal growth by a modified Bridgman technique. *Mater. Res. Bull.* **2014**, *60*, 819–823.
- (24) García-Martínez, O.; Rojas, R. M.; Vila, E.; Martín de Vidales, J. L. Microstructural characterization of nanocrystals of ZnO and CuO obtained from basic salts. *Solid State Ionics* **1993**, *63–65*, 442.
- (25) Lopez, F. A.; Lopez-Delgado, A.; Martín de Vidales, J. L.; Vila, E. Synthesis of nanocrystalline zinc ferrite powders from sulphuric pickling waste water. *J. Alloys Compd.* **1998**, *265*, 291–296.
- (26) Mehrani, A.; Mehrani, K. Synthesis of ZnFe₂O₄ Nanoparticles Confined Within Nanoporous Silica Using Trinuclear Oxo-centered Complex: Inorganic Complexes as a Precursor for the Preparation of Magnetic Nanoporous Silica. *J. Inorg. Organomet. Polym. Mater.* **2012**, *22*, 1419–1424.
- (27) Cao, G.; Subedi, A.; Calder, S.; Yan, J.-Q.; Yi, J.; Gai, Z.; Poudel, L.; Singh, D. J.; Lumsden, M. D.; Christianson, A. D.; Sales, B. C.; Mandrus, D. Magnetism and electronic structure of La₂ZnIrO₆ and La₂MgIrO₆: Candidate J_{eff} = 1/2 Mott insulators. *Phys. Rev. B: Condens. Matter Mater. Phys.* **2013**, *87*, 155136.
- (28) Demazeau, G.; Jung, D. Y.; Largeteau, A.; Cros, C.; Choy, J. H. High oxygen pressures and the stabilization of the highest oxidation states of transition elements. *J. Alloys Compd.* **1997**, *262–263*, 191–193.
- (29) Ou, X.; Li, Z.; Fan, F.; Wang, H.; Wu, H. Long-Range Magnetic Interaction and Frustration in Double Perovskites Sr₂NiIrO₆ and Sr₂ZnIrO₆. *Sci. Rep.* **2015**, *4*, 7542.
- (30) Kayser, P.; Martínez-Lope, M. J.; Alonso, J. A.; Retuerto, M.; Croft, M.; Ignatov, A.; Fernández-Díaz, M. T. Crystal Structure, Phase Transitions, and Magnetic Properties of Iridium Perovskites Sr₂MIrO₆ (M = Ni, Zn). *Inorg. Chem.* **2013**, *52*, 11013–11022.
- (31) Altomare, A.; Cuocci, C.; Giacovazzo, C.; Moliterni, A.; Rizzi, R.; Corriero, N.; Falcicchio, A. EXPO2013: a kit of tools for phasing crystal structures from powder data. *J. Appl. Crystallogr.* **2013**, *46*, 1231–1235.
- (32) Larson, A. C.; Von Dreele, R. B. General Structure Analysis System (GSAS). Technical Report LAUR 86-748; Los Alamos National Laboratory: Los Alamos, NM, 1994.
- (33) Christy, A. G.; Mills, S. J.; Kampf, A. R. A review of the structural architecture of tellurium oxycompounds. *Mineral. Mag.* **2016**, *80* (3), 415–545.
- (34) Shannon, R. D. Revised Effective Ionic Radii and Systematic Studies of Interatomic Distances in Halides and Chalcogenides. *Acta Crystallogr., Sect. A: Cryst. Phys., Diffr., Theor. Gen. Crystallogr.* **1976**, *32*, 751.
- (35) Khalid, M.; Setzer, A.; Ziese, M.; Esquinazi, P.; Spemann, D.; Pöpl, A.; Goering, E. Ubiquity of ferromagnetic signals in common diamagnetic oxide crystals. *Phys. Rev. B: Condens. Matter Mater. Phys.* **2010**, *81*, 214414.
- (36) Zhang, J.; Shi, F.; Lin, J.; Chen, D.; Gao, J.; Huang, Z.; Ding, X.; Tang, C. Self-Assembled 3-D Architectures of BiOBr as a Visible Light-Driven Photocatalyst. *Chem. Mater.* **2008**, *20*, 2937–2941.
- (37) Yamanaka, S.; Kurosaki, K.; Oyama, T.; Muta, H.; Uno, M.; Matsuda, T.; Kobayashi, S. Thermophysical Properties of Perovskite-Type Strontium Cerate and Zirconate. *J. Am. Ceram. Soc.* **2005**, *88*, 1496.

(38) Fousek, J. Ferroelectricity: Remarks on historical aspects and present trends. *Ferroelectrics* **1991**, *113*, 3–20.

(39) Dammak, M.; Khemakhem, H.; Mhiri, T. Superprotonic conduction and ferroelectricity in addition cesium sulfate tellurate $\text{Cs}_2\text{SO}_4\text{Te}(\text{OH})_6$. *J. Phys. Chem. Solids* **2001**, *62*, 2069–2074.

(40) Liebmann, M.; Rinaldi, C.; Di Sante, D.; Kellner, J.; Pauly, C.; Wang, R. N.; Boschker, J. E.; Giussani, A.; Bertoli, S.; Cantoni, M.; Baldrati, L.; Asa, M.; Vobornik, I.; Panaccione, G.; Marchenko, D.; Sánchez-Barriga, J.; Rader, O.; Calarco, R.; Picozzi, S.; Bertacco, R.; Morgenstern, M. Giant Rashba-type spin splitting in ferroelectric $\text{GeTe}(111)$. *Adv. Mater.* **2016**, *28*, 560–565.